Research Square

Preprints are preliminary reports that have not undergone peer review.
They should not be considered conclusive, used to inform clinical practice,
or referenced by the media as validated information.

Identification of a non-thermal X-ray burst with the Galactic magnetar SGR J1935+2154 and a fast radio burst using Insight-HXMT

C.K. Li
Institute of High Energy Physics, Chinese Academy of Sciences https://orcid.org/0000-0001-5798-4491
Lin Lin
Beijing Normal University
S.L. Xiong
Institute of High Energy Physics, Chinese Academy of Sciences
Mingyu Ge
Institute of High Energy Physics, Chinese Academy of Sciences
X.B. Li
Institute of High Energy Physics, Chinese Academy of Sciences, 19B Yuquan Road, Beijing 100049,People's Republic of China
Tipei Li
Tsinghua University
F.J. Lu
Institute of High Energy Physics, Chinese Academy of Sciences, 19B Yuquan Road, Beijing 100049,People's Republic of China
Shuang-Nan Zhang (zhangsn@ihep.ac.cn)
Institute of High Energy Physics, Chinese Academy of Sciences, 19B Yuquan Road, Beijing 100049,People's Republic of China https://orcid.org/0000-0001-5586-1017
Y.L. Tuo
Institute of High Energy Physics, Chinese Academy of Sciences, 19B Yuquan Road, Beijing 100049,People's Republic of China https://orcid.org/0000-0003-3127-0110
Y. Nang
Institute of High Energy Physics, Chinese Academy of Sciences, 19B Yuquan Road, Beijing 100049,People's Republic of China
B. Zhang
University of Nevada, Las Vegas
S. Xiao
Institute of High Energy Physics, Chinese Academy of Sciences, 19B Yuquan Road, Beijing 100049,People's Republic of China

Y. Chen
Institute of High Energy Physics, Chinese Academy of Sciences, 19B Yuquan Road, Beijing 100049,People's Republic of China
L.M. Song
Institute of High Energy Physics, Chinese Academy of Sciences, 19B Yuquan Road, Beijing 100049,People's Republic of China
Y.P. Xu
Institute of High Energy Physics, Chinese Academy of Sciences, 19B Yuquan Road, Beijing 100049,People's Republic of China https://orcid.org/0000-0002-8476-9217
C.Z. Liu
Institute of High Energy Physics, Chinese Academy of Sciences, 19B Yuquan Road, Beijing 100049,People's Republic of China
S.M. Jia
Institute of High Energy Physics, Chinese Academy of Sciences
X.L. Cao
Institute of High Energy Physics, Chinese Academy of Sciences, 19B Yuquan Road, Beijing 100049,People's Republic of China
J.L. Qu
Institute of High Energy Physics, Chinese Academy of Sciences, 19B Yuquan Road, Beijing 100049,People's Republic of China
Shu Zhang
Laboratory for Particle Astrophysics, IHEP
Y.D. Gu
Technology and Engineering Center for Space Utilization, Chinese Academy of Sciences
J.Y. Liao
Institute of High Energy Physics, Chinese Academy of Sciences, 19B Yuquan Road, Beijing 100049,People's Republic of China
X.F. Zhao
Institute of High Energy Physics, Chinese Academy of Sciences, 19B Yuquan Road, Beijing 100049,People's Republic of China
Y. Tan
Institute of High Energy Physics, Chinese Academy of Sciences, 19B Yuquan Road, Beijing 100049,People's Republic of China
J.Y. Nie
Institute of High Energy Physics, Chinese Academy of Sciences, 19B Yuquan Road, Beijing 100049,People's Republic of China
H.S. Zhao
Institute of High Energy Physics, Chinese Academy of Sciences, 19B Yuquan Road, Beijing 100049,People's Republic of China
S.J. Zheng

Institute of High Energy Physics, Chinese Academy of Sciences, 19B Yuquan Road, Beijing 100049,People's Republic of China

Y.G. Zheng

Institute of High Energy Physics, Chinese Academy of Sciences, 19B Yuquan Road, Beijing 100049,People's Republic of China

Qi Luo

Institute of High Energy Physics https://orcid.org/0000-0003-1853-7810

C. Cai

Institute of High Energy Physics, Chinese Academy of Sciences, 19B Yuquan Road, Beijing 100049,People's Republic of China

B. Li

Institute of High Energy Physics, Chinese Academy of Sciences, 19B Yuquan Road, Beijing 100049,People's Republic of China https://orcid.org/0000-0002-0238-834X

W.C. Xue

Institute of High Energy Physics, Chinese Academy of Sciences, 19B Yuquan Road, Beijing 100049,People's Republic of China

Qingcui Bu

Institute of High Energy Physics, Chinese Academy of Sciences https://orcid.org/0000-0001-5238-3988

Zhi Chang

Institute of High Energy Physics https://orcid.org/0000-0003-4856-2275

G. Chen

Institute of High Energy Physics, Chinese Academy of Sciences, 19B Yuquan Road, Beijing 100049,People's Republic of China

T.X. Chen

Institute of High Energy Physics, Chinese Academy of Sciences, 19B Yuquan Road, Beijing 100049,People's Republic of China

Yu-Peng Chen

IHEP

Yong-Wei Dong

Institute of High Energy Physics, Chinese Academy of Sciences https://orcid.org/0000-0003-3882-8316

Y.Y. Du

Institute of High Energy Physics, Chinese Academy of Sciences, 19B Yuquan Road, Beijing 100049,People's Republic of China

H. Gao

Institute of High Energy Physics, Chinese Academy of Sciences, 19B Yuquan Road, Beijing 100049,People's Republic of China

G.H. Gao

Institute of High Energy Physics, Chinese Academy of Sciences, 19B Yuquan Road, Beijing 100049,People's Republic of China
M. Gao
Institute of High Energy Physics, Chinese Academy of Sciences, 19B Yuquan Road, Beijing 100049,People's Republic of China
Y.D. Gu
Institute of High Energy Physics, Chinese Academy of Sciences, 19B Yuquan Road, Beijing 100049,People's Republic of China
J. Huo
Institute of High Energy Physics, Chinese Academy of Sciences, 19B Yuquan Road, Beijing 100049,People's Republic of China
D.W. Han
Institute of High Energy Physics, Chinese Academy of Sciences, 19B Yuquan Road, Beijing 100049,People's Republic of China
L.H. Jiang
Institute of High Energy Physics, Chinese Academy of Sciences, 19B Yuquan Road, Beijing 100049,People's Republic of China
Y. Huang
Institute of High Energy Physics, Chinese Academy of Sciences, 19B Yuquan Road, Beijing 100049,People's Republic of China
Weichun Jiang
IHEP
J. Jin
Institute of High Energy Physics, Chinese Academy of Sciences, 19B Yuquan Road, Beijing 100049,People's Republic of China
L.D. Kong
Institute of High Energy Physics, Chinese Academy of Sciences, 19B Yuquan Road, Beijing 100049,People's Republic of China
Gang Li
Institute of High Energy Physics
J. Guan
Institute of High Energy Physics, Chinese Academy of Sciences
M.S. Li
Institute of High Energy Physics, Chinese Academy of Sciences, 19B Yuquan Road, Beijing 100049,People's Republic of China
W. Li
Institute of High Energy Physics, Chinese Academy of Sciences, 19B Yuquan Road, Beijing 100049,People's Republic of China
X. Li

Institute of High Energy Physics, Chinese Academy of Sciences, 19B Yuquan Road, Beijing 100049,People's Republic of China

X.F. Li

Institute of High Energy Physics, Chinese Academy of Sciences, 19B Yuquan Road, Beijing 100049,People's Republic of China https://orcid.org/0000-0002-2793-9857

Y.G. Li

Institute of High Energy Physics, Chinese Academy of Sciences, 19B Yuquan Road, Beijing 100049,People's Republic of China

Z.W. Li

Institute of High Energy Physics, Chinese Academy of Sciences, 19B Yuquan Road, Beijing 100049,People's Republic of China

X.H. Liang

Institute of High Energy Physics, Chinese Academy of Sciences, 19B Yuquan Road, Beijing 100049,People's Republic of China

B.S. Liu

Institute of High Energy Physics, Chinese Academy of Sciences, 19B Yuquan Road, Beijing 100049,People's Republic of China

H.W. Liu

Institute of High Energy Physics, Chinese Academy of Sciences, 19B Yuquan Road, Beijing 100049,People's Republic of China

X.J. Liu

Institute of High Energy Physics, Chinese Academy of Sciences, 19B Yuquan Road, Beijing 100049,People's Republic of China

B. Lu

Institute of High Energy Physics, Chinese Academy of Sciences, 19B Yuquan Road, Beijing 100049,People's Republic of China

X.F. Lu

Institute of High Energy Physics, Chinese Academy of Sciences, 19B Yuquan Road, Beijing 100049,People's Republic of China

T. Luo

Institute of High Energy Physics, Chinese Academy of Sciences, 19B Yuquan Road, Beijing 100049,People's Republic of China

X. Ma

Institute of High Energy Physics, Chinese Academy of Sciences, 19B Yuquan Road, Beijing 100049,People's Republic of China

B. Meng

Institute of High Energy Physics, Chinese Academy of Sciences, 19B Yuquan Road, Beijing 100049,People's Republic of China

G. Ou

Institute of High Energy Physics, Chinese Academy of Sciences, 19B Yuquan Road, Beijing 100049,People's Republic of China https://orcid.org/0000-0002-3188-9063

N. Sai

Institute of High Energy Physics, Chinese Academy of Sciences, 19B Yuquan Road, Beijing 100049,People's Republic of China https://orcid.org/0000-0001-8378-5904

X.Y. Song

Institute of High Energy Physics, Chinese Academy of Sciences, 19B Yuquan Road, Beijing 100049,People's Republic of China

L. Sun

Institute of High Energy Physics, Chinese Academy of Sciences, 19B Yuquan Road, Beijing 100049,People's Republic of China

Lian Tao

Institute of High Energy Physics, Chinese Academy of Sciences https://orcid.org/0000-0002-2705-4338

J. Wang

Institute of High Energy Physics, Chinese Academy of Sciences, 19B Yuquan Road, Beijing 100049,People's Republic of China

G.F. Wang

Institute of High Energy Physics, Chinese Academy of Sciences, 19B Yuquan Road, Beijing 100049,People's Republic of China

W.S. Wang

Institute of High Energy Physics, Chinese Academy of Sciences, 19B Yuquan Road, Beijing 100049,People's Republic of China

Y.S. Wang

Institute of High Energy Physics, Chinese Academy of Sciences, 19B Yuquan Road, Beijing 100049,People's Republic of China

X.Y. Wen

Institute of High Energy Physics, Chinese Academy of Sciences, 19B Yuquan Road, Beijing 100049,People's Republic of China

B.B. Wu

Institute of High Energy Physics, Chinese Academy of Sciences, 19B Yuquan Road, Beijing 100049,People's Republic of China

B.Y. Wu

Institute of High Energy Physics, Chinese Academy of Sciences, 19B Yuquan Road, Beijing 100049,People's Republic of China

M. Wu

Institute of High Energy Physics, Chinese Academy of Sciences, 19B Yuquan Road, Beijing 100049,People's Republic of China

G.C. Xiao

Institute of High Energy Physics, Chinese Academy of Sciences, 19B Yuquan Road, Beijing 100049,People's Republic of China
H. Xu
Institute of High Energy Physics, Chinese Academy of Sciences, 19B Yuquan Road, Beijing 100049,People's Republic of China
J.W. Yang
Institute of High Energy Physics
S. Yang
Institute of High Energy Physics, Chinese Academy of Sciences, 19B Yuquan Road, Beijing 100049,People's Republic of China
Yi-Jung Yang
Institute of High Energy Physics, Chinese Academy of Sciences, 19B Yuquan Road, Beijing 100049,People's Republic of China
Y.J. Yang
Institute of High Energy Physics, Chinese Academy of Sciences, 19B Yuquan Road, Beijing 100049,People's Republic of China
Q.B. Yi
Institute of High Energy Physics, Chinese Academy of Sciences, 19B Yuquan Road, Beijing 100049,People's Republic of China
Q.Q. Yin
Institute of High Energy Physics, Chinese Academy of Sciences, 19B Yuquan Road, Beijing 100049,People's Republic of China
Y. You
Institute of High Energy Physics, Chinese Academy of Sciences, 19B Yuquan Road, Beijing 100049,People's Republic of China
C.M. Zhang
Institute of High Energy Physics, Chinese Academy of Sciences, 19B Yuquan Road, Beijing 100049,People's Republic of China
A.M. Zhang
Institute of High Energy Physics, Chinese Academy of Sciences, 19B Yuquan Road, Beijing 100049,People's Republic of China
F. Zhang
Institute of High Energy Physics, Chinese Academy of Sciences, 19B Yuquan Road, Beijing 100049,People's Republic of China
H.M. Zhang
Institute of High Energy Physics, Chinese Academy of Sciences, 19B Yuquan Road, Beijing 100049,People's Republic of China
J. Zhang

Institute of High Energy Physics, Chinese Academy of Sciences, 19B Yuquan Road, Beijing 100049,People's Republic of China
T. Zhang
Institute of High Energy Physics, Chinese Academy of Sciences, 19B Yuquan Road, Beijing 100049,People's Republic of China
Wei Zhang
Key Laboratory of Particle Astrophysics, Institute of High Energy Physics, Chinese Academy of Sciences
W.C. Zhang
Institute of High Energy Physics, Chinese Academy of Sciences, 19B Yuquan Road, Beijing 100049,People's Republic of China
Y. Zhang
Institute of High Energy Physics, Chinese Academy of Sciences, 19B Yuquan Road, Beijing 100049,People's Republic of China
Yue Zhang
Institute of High Energy Physics, Chinese Academy of Sciences, 19B Yuquan Road, Beijing 100049,People's Republic of China
Y.F. Zhang
Institute of High Energy Physics, Chinese Academy of Sciences, 19B Yuquan Road, Beijing 100049,People's Republic of China
Y.J. Zhang
Institute of High Energy Physics, Chinese Academy of Sciences, 19B Yuquan Road, Beijing 100049,People's Republic of China
Z.L. Zhang
Institute of High Energy Physics, Chinese Academy of Sciences, 19B Yuquan Road, Beijing 100049,People's Republic of China
D.K. Zhou
Institute of High Energy Physics, Chinese Academy of Sciences, 19B Yuquan Road, Beijing 100049,People's Republic of China
Y. Zhu
Institute of High Energy Physics, Chinese Academy of Sciences, 19B Yuquan Road, Beijing 100049,People's Republic of China
Y.X. Zhu
Institute of High Energy Physics, Chinese Academy of Sciences, 19B Yuquan Road, Beijing 100049,People's Republic of China
L. Chen
Beijing Normal University
W.Z. Zhang
Beijing Normal University
Y.B. Chen

Tsinghua University
W. Cui
Tsinghua University https://orcid.org/0000-0002-6324-5772
J.K. Deng
Tsinghua University
M.X. Fu
Tsinghua University
Y.J. Jin
Tsinghua University
G.Q. Liu
Tsinghua University
Y.N. Liu
Tsinghua University
R.C. Shang
Tsinghua University
Zhao Zhang
Tsinghua University
Zhi Zhang
Tsinghua University
J.F. Zhou
Tsinghua University
C. Wang
National Astronomical Observatories, Chinese Academy of Sciences https://orcid.org/0000-0003-3927-3965
C.C. Guo
Institute of High Energy Physics, Chinese Academy of Sciences
R.L. Zhuang
Tsinghua University

Research Article

Keywords: Fast Radio Bursts, Non-thermal X-Ray burst

Posted Date: August 28th, 2020

DOI: https://doi.org/10.21203/rs.3.rs-62191/v1

License: This work is licensed under a Creative Commons Attribution 4.0 International License.
Read Full License

Version of Record: A version of this preprint was published at Nature Astronomy on February 18th, 2021. See the published version at https://doi.org/10.1038/s41550-021-01302-6.

Identification of a non-thermal X-ray burst with the Galactic magnetar SGR J1935+2154 and a fast radio burst using *Insight*-HXMT

C.K. Li[1†], L. Lin[2†], S.L. Xiong[1†], M.Y. Ge[1], X.B. Li[1], T.P. Li[1,3,4‡], F.J. Lu[1‡], S.N. Zhang[1,3‡], Y.L. Tuo[1,3], Y. Nang[1,3], B. Zhang[5], S. Xiao[1,3], Y. Chen[1], L.M. Song[1,3], Y.P. Xu[1,3], C.Z. Liu[1], S.M. Jia[1], X.L. Cao[1], J.L. Qu[1], S. Zhang[1], Y.D. Gu[6], J.Y. Liao[1], X.F. Zhao[1,3], Y. Tan[1], J.Y. Nie[1], H.S. Zhao[1], S.J. Zheng[1], Y.G. Zheng[1,12], Q. Luo[1,3], C. Cai[1,3], B. Li[1], W.C. Xue[1], Q.C. Bu[1,7], Z. Chang[1], G. Chen[8], L. Chen[2], T.X. Chen[1], Y.B. Chen[9], Y.P. Chen[1], W. Cui[4], W.W. Cui[1], J.K. Deng[10], Y.W. Dong[1], Y.Y. Du[1], M.X. Fu[10], G.H. Gao[1,3], H. Gao[1,3], M. Gao[1], Y.D. Gu[1], J. Guan[1], C.C. Guo[1,3], D.W. Han[1], Y. Huang[1], J. Huo[1], L.H. Jiang[1], W.C. Jiang[1], J. Jin[1], Y.J. Jin[10], L.D. Kong[1,3], G. Li[1], M.S. Li[1], W. Li [1], X. Li[1], X.F. Li[1], Y.G. Li[1], Z.W. Li[1], X.H. Liang[1], B.S. Liu[1], G.Q. Liu[9], H.W. Liu[8], X.J. Liu[1], Y.N. Liu[10], B. Lu[1], X.F. Lu[1], T. Luo[1], X. Ma[1], B. Meng[1], G. Ou[11], N. Sai[1,3], R.C. Shang[9], X.Y. Song[1], L. Sun[1], L. Tao[1], C. Wang[12,3], G.F. Wang[1], J. Wang[1], W.S. Wang[11], Y.S. Wang[1], X.Y. Wen[1], B.B. Wu[1], B.Y. Wu[1,3], M. Wu[1], G.C. Xiao[1,3], H. Xu[1], J.W. Yang[1], S. Yang[1], Y.J. Yang[1], Yi-Jung Yang[1], Q.B. Yi[1,14], Q.Q. Yin[1], Y. You[1,3], A.M. Zhang[1], C.M. Zhang[1], F. Zhang[8], H.M. Zhang[11], J. Zhang[1], T. Zhang[1], W. Zhang[1,3], W.C. Zhang[1], W.Z. Zhang[2], Y. Zhang[1], Yue Zhang[1,3], Y.F. Zhang[1], Y.J. Zhang[1], Z. Zhang[9], Zhi Zhang[10], Z.L. Zhang[1], D.K. Zhou[1,3], J.F. Zhou[10], Y. Zhu[1], Y.X. Zhu[1,15], R.L. Zhuang[10] (the *Insight*-HXMT team)

[1]*Key Laboratory of Particle Astrophysics, Institute of High Energy Physics, Chinese Academy of Sciences, 19B Yuquan Road, Beijing 100049, China*

[2]*Department of Astronomy, Beijing Normal University, Beijing 100875, China*

[3]*University of Chinese Academy of Sciences, Chinese Academy of Sciences, Beijing 100049, China*

[4]*Department of Astronomy, Tsinghua University, Beijing 100084, China*

[5]*Department of Physics and Astronomy, University of Nevada, Las Vegas, NV 89154, USA*

[6]*Technology and Engineering Center for Space Utilization, Chinese Academy of Sciences, Beijing 100094, China*

[7]*Institut für Astronomie und Astrophysik, Kepler Center for Astro and Particle Physics, Eberhard Karls Universität, Sand 1, 72076 Tübingen, Germany*

[8]*Institute of High Energy Physics, Chinese Academy of Sciences, 19B Yuquan Road, Beijing 100049, China*

†Co-First Authors. These authors contributed equally and are in alphabetical order: Cheng-Kui Li, Lin Lin and Shao-Lin Xiong

‡Co-Corresponding Authors. These authors contributed equally and are in alphabetical order: Ti-Pei Li, Fang-Jun Lu and Shuang-Nan Zhang

[9] *Department of Physics, Tsinghua University, Beijing 100084, China*
[10] *Department of Engineering Physics, Tsinghua University, Beijing 100084, China*
[11] *Computing Division, Institute of High Energy Physics, Chinese Academy of Sciences, 19B Yuquan Road, Beijing 100049, China*
[12] *Key Laboratory of Space Astronomy and Technology, National Astronomical Observatories, Chinese Academy of Sciences, Beijing 100012, China*
[13] *College of physics Sciences and Technology, Hebei University, Baoding City, Hebei Province, 071002, China*
[14] *School of Physics and Optoelectronics, Xiangtan University, Xiangtan City, Hunan Province, 411105, China*
[15] *College of Physics, Jilin University, Changchun City, Jilin Province, 130012, China*

Fast radio bursts (FRBs) are short pulses observed in radio band from cosmological distances[1], some of which emit repeating bursts[2]. The physical origins of these mysterious events have been subject to wide speculations and heated debates. One class of models invoke soft gamma-ray repeaters (SGRs), or magnetars, as the sources of FRBs[3]. Magnetars are rotating neutron stars with extremely strong magnetic field[4] and can sporadically emit bursts from X-ray (∼keV) to soft gamma-ray (∼sub-MeV) with duration[5] from 10^{-2} s to 10^{2} s. However, even though some bright radio bursts have been observed from some magnetars[6], no FRB-like events had been detected to be associated with any magnetar burst, including one giant flare[7], and no radio burst has been associated with any X-ray event from any magnetar. Therefore, there is still no observational evidence for magnetar-FRB association up to today. Recently, a pair of FRB-like bursts (FRB 200428 hereafter) separated by 30 milliseconds (ms) were detected from the general direction of the Galactic magnetar SGR J1935+2154[8,9]. Here we report the detection of a non-thermal X-ray burst in the 1–250 keV energy band with the *Insight*-HXMT satellite[10], which we identify as emitted from SGR J1935+2154. The burst showed two hard peaks with a separation of ~ 30 ms, consistent with the separation between the two bursts in FRB 200428. The delay time between the double radio and X-ray peaks is ~ 8.57 s, fully consistent with the dispersion delay of FRB 200428. We thus identify the non-thermal X-ray burst is associated with FRB 200428 whose high energy counterpart is the two hard peaks in X-ray. Our results suggest that the non-thermal X-ray burst and FRB 200428 share the same physical origin in an explosive event from SGR J1935+2154.

SGR J1935+2154 was discovered when it went into outburst in 2014[11]. Since then and before 2020, the source experienced several activities in 2015 February, 2016 May to July and 2019 November[12,13]. Between outbursts, isolated bright flares or short bursts in X-ray or gamma-ray have been detected from the source[13,14]. These make SGR J1935+2154 one of the most active magnetars. Starting from 2020 April 27 18:26:20 UT, a series of X-ray and gamma-ray instruments were triggered by multiple short bursts and a burst forest including hundreds of bursts from SGR J1935+2154[15,16]. Within thirteen hours, we started a long Target of Opportunity (ToO) observation of this source using *Insight*-HXMT with all its three collimated telescopes covering 1–10 keV (Low Energy X-ray telescope, LE), 5–30 keV (Medium Energy X-ray telescope, ME) and 20–250 keV (High Energy X-ray telescope, HE), respectively. This pointed ToO observation continued for 60 ks from April 28 07:14:52 UT to April 29 11:53:01 UT.

During the *Insight*-HXMT observation, a double-peaked and short radio burst, FRB 200428, from the general direction of SGR J1935+2154 was reported by CHIME/FRB[8] and STARE2[9] at April 28 UTC 14:34:33 (at 400 MHz) and 14:34:25 (at 1.4 GHz), respectively. The fluence of this radio burst recorded by STARE2[9] is > 1.5 MJy ms , which is over six magnitudes brighter than those radio bursts from XTE J1810-197[6], which had been the brightest radio bursts from magnetars. This makes it the first possible magnetar radio burst detectable from an extra-galactic distance (e.g FRB 180916.J0158+65 at 149 Mpc[9]), if FRB 200428 were emitted from SGR J1935+2154.

Insight-HXMT detected a series of 11 bursts within about 17 hours of exposure to SGR J1935+2154 (see **Methods** for description and burst list). It is mostly likely that most, if not all, of these bursts came from SGR J1935+2154, since it was the only active magnetar in this period and in the field of view of *Insight*-HXMT. The brightest burst with a trigger time (denoted as T_0) of April 28 14:34:24.0000 UT (satellite time) or 14:34:24.0114 UT (geocentric time) lasted for about 1 second in 1–250 keV and was seen clearly in all three telescopes. This burst is also the closest one in time to FRB 200428. With different orientations of the collimators, *Insight*-HXMT can localize the burst within its field of view, as shown in Figure 1. The burst is located at $\mathrm{RA} = 293.67^{+0.16}_{-0.11}$ deg, $\mathrm{Dec} = 21.92^{+0.08}_{-0.07}$ deg, ~3.7 arcmin away from SGR J1935+2154 with 1σ error of ~10 arcmin. We thus identify this burst as coming from SGR J1935+2154.

This burst was so bright that it saturated both LE and HE, and also caused moderate deadtime effects in ME. After correcting all these effects (see **Methods**), the lightcurves and hardness of the burst obtained by the three telescopes are presented in Figure 2. The full lightcurves of this burst consist of two major bumps separated by about 0.2 s, and a minor soft bump just before T_0 that is only present in LE and ME data, indicating overall spectral evolution as shown by the hardness evolution during the burst. The second major bump, which was also detected by INTEGRAL[17] and Konus-Wind[18], is much brighter than the first one. In the lightcurves of both ME and HE, two narrow peaks are clearly seen (see **Methods**) during the second major bump. In the LE lightcurve, only the second narrow peak is visible significantly, indicating somewhat different broad band energy spectra between the two narrow peaks. The separation time between the two narrow X-ray

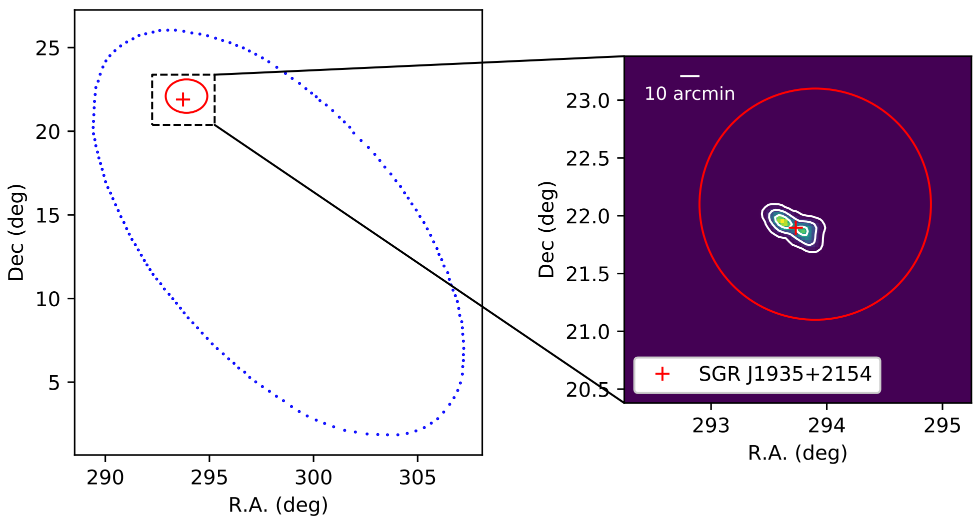

Figure 1: Localization of the burst using *Insight*-HXMT HE, ME and LE data. The red cross marks the known position of SGR J1935+2154. The white contours in the zoomed in panel are 1σ, 2σ and 3σ uncertainty regions in the sky. The best position of this burst is $\sim$3.7 arcmin away from SGR J1935+2154 with 1σ error of $\sim$10 arcmin (see **Methods** for details about localization). The red circle and blue-dotted ellipse presents the sky region of FRB 200428 determined by CHIME/FRB[8] and STARE2[9], respectively.

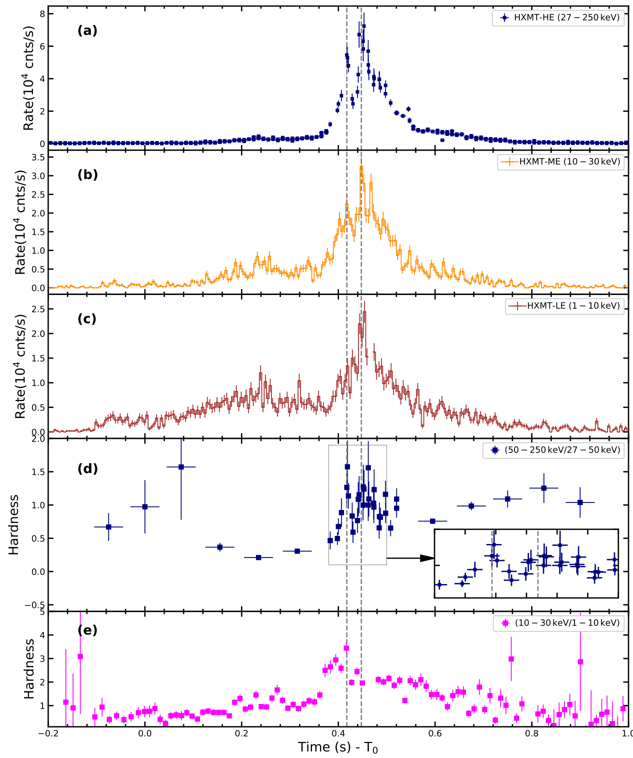

Figure 2: The lightcurve and the hardness evolution during the burst of SGR J1935+2145 observed with *Insight*-HXMT. The reference time is T_0 (2020-04-28 14:34:24 UTC). The vertical dashed lines indicate two peaks in the lightcurves and the hardness evolution. The separation between the two lines are 30 ms. **(a)**: The lightcurve observed with *Insight*-HXMT/HE with a time resolution of 1 ms near the peak and 10 ms outside the peak. Due to the saturation effect, there are bins near the peak with no photons recorded for both HE and LE. **(b)** and **(c)** are the lightcurves observed with ME and LE with a time bin of 5 ms, respectively. **(d)**: The hardness ratio between the counts in 50–250 keV and 27–50 keV. The inset plot in **(d)** shows the details of the hardness ratio near the peak. **(e)**: The hardness ratio between the counts in 10–30 keV and the 1–10 keV. (see **Methods** for details of the saturation and the deadtime correction.)

peaks ($\sim$ 30 ms) is consistent with that of the two narrow peaks in FRB 200428, and the apparent time lag between X-ray and radio peaks ($\sim$8.57 s) is in good agreement with the calculated dispersion delay (8.63 s) between X-ray and radio using the DM ($\sim$333 pc/cm^3) measured by CHIME/FRB[8] and STARE2[9]. We thus identify the burst detected by *Insight*-HXMT is associated with FRB 200428 and both belong to a single explosive event from SGR J1935+2154.

The time-integrated spectrum of this burst ($T_0 - 0.2$ s to $T_0 + 1.0$ s) is derived jointly using HE, ME and LE data (Figure 3, see **Methods** for details of spectral fitting). The best fit and statistically acceptable model is a cutoff power-law (CPL) with neutral hydrogen column density $n_{\rm H} = (2.79^{+0.18}_{-0.17}) \times 10^{22}$ cm^{-2}, photon index $\Gamma = 1.56 \pm 0.06$ and cutoff energy $E_{\rm cut} = 83.89^{+9.08}_{-7.55}$ keV (corresponding to a peak energy $E_{\rm peak} = (2 - \Gamma)E_{\rm cut} \sim 37$ keV). The unabsorbed fluence is $(7.14^{+0.41}_{-0.38}) \times 10^{-7}$ erg cm^{-2} in 1–250 keV, corresponding to a total emission energy of $\sim 1 \times 10^{40}$ erg for the 12.5 kpc[19] distance of SGR J1935+2154. This burst is brighter than $\sim 84\%$ of events collected from the source during $2014 - 2016$ with *Fermi*/GBM[13]. We also fit the spectrum with several other spectral models, e.g., single power-law (PL), double blackbody (BB+BB) and blackbody plus power-law (BB+PL). The fit to the BB+PL mode is marginally consistent with data, with slightly higher column density ($n_{\rm H} = (3.50 \pm 0.17) \times 10^{22}$ cm^{-2}) and larger photon index ($\Gamma = 1.93 \pm 0.04$); the flux of the unabsorbed blackbody component with temperature of $11.32^{+0.55}_{-0.56}$ keV is only 18% of the total flux in 1–250 keV. The other two models provide significantly worse fit and are thus rejected.

We conclude that the integrated spectrum is dominated by a power-law covering at least the 1-100 keV range, and thus this burst is primarily non-thermal in nature. It is also clear that the two narrow peaks separated by $\sim$ 30 ms must also be dominated by a non-thermal spectrum, since the hardness reaches its maximum during the peak of the second bump of the lightcurves where the two narrow peaks are found. It is interesting to note that the lower limit of the radio flux detected with STARE2[9] falls in between the extrapolated values from the non-thermal X-ray spectrum with the power-law parameters of the fits to the CPL and BB+PL models (see the panel (f) in Figure 3).

In summary, with the observation of *Insight*-HXMT we have identified that the short non-thermal X-ray burst was emitted by the Galactic magnetar SGR J1935+2154 and produced almost simultaneously with FRB 200428 in a single explosive event. In the literature, FRB emission has been interpreted as either coherent curvature radiation of electron-positron pairs from a neutron star magnetosphere[20–22] or synchrotron maser emission in a relativistic, magnetized shock[23,24]. Since magnetar bursts are believed to be magnetosphere-related[25], the fact that the narrow double peaks in both radio and X-ray are emitted around the same time, and hence, likely originate from the same emission region, lends support to the magnetospheric models of FRBs.

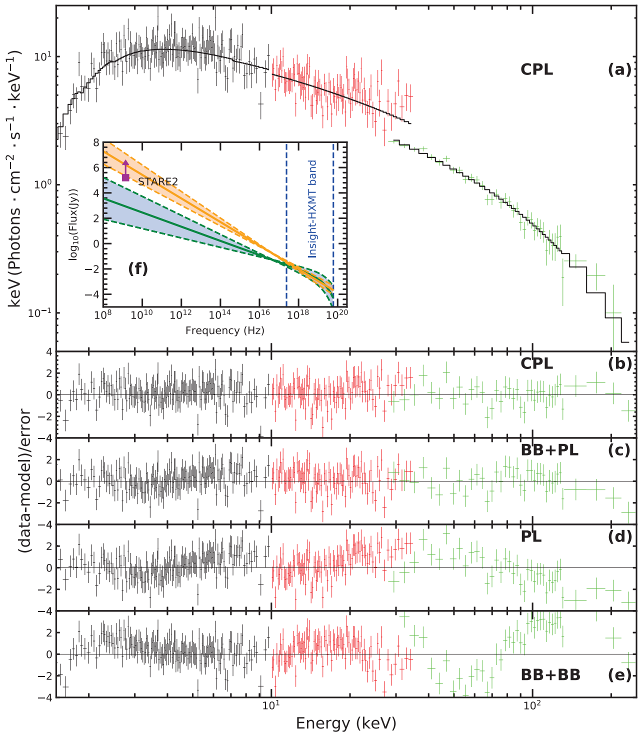

Figure 3: The spectrum observed with *Insight*-HXMT covers the 1–250 keV energy band. Data from the three telescopes of *Insight*-HXMT covering different energy bands are represented in different colors (LE: black, ME: red and HE: green). In the fitting process, we introduced a constant factor to offset the different saturation and deadtime effects in different detectors. Four models were considered, cutoff power-law (CPL), blackbody+power-law (BB+PL), power-law (PL), and blackbody+blackbody (BB+BB). The equivalent hydrogen column in the interstellar absorption model was free to fit. **(a)** The X-ray spectrum of SGR J1935+2154 described by CPL model. The inset (**f**) shows the comparison between the radio flux lower limit detected with STARE2[9] and extrapolations from the X-ray spectrum to the radio frequency range, where the green and orange regions are the 3σ error bands with the parameters of the CPL (below STARE2) and BB+PL (above STARE2) models, respectively. Panels **(b)**-**(e)** are the residuals of the data from the individual models, respectively. (see **Methods** for details of the spectral fitting and parameters derived.)

However, a thermal origin is preferred for normal short bursts from magnetars[26,27]. We notice that $\sim 6\%$ of the bursts ($7/109$) from SGR J1935+2154 detected with Fermi/GBM between 2014 and 2016 can be best fit with a power-law model[13]. The fluence of these bursts is about one order of magnitude dimmer than this one associated with FRB 200428. We therefore set a conservative upper limit of 6% to the percentage of magnetar bursts which may have similar radio emission to FRB 200428. Actually, non-thermal X-ray bursts are very rarely observed from magnetars in general, which explains why events similar to FRB 200428 have not been seen previously.

Previously we have conducted a search for prompt γ-ray counterparts to FRBs[28] in the Insight-HXMT data and obtained only lower limits as low as 5.5×10^{47} erg s^{-1} over 1 s for the periodic repeater FRB 180916.J0158+65. If this X-ray burst were emitted from an extragalactic magnetar located at a distance of FRB 180916.J0158+65 at 149 Mpc[29], and assume the distance of SGR J1935+2154 is 12.5 kpc[19], then the observed fluence should be $\sim 4 \times 10^{-15}\ \mathrm{erg\ cm^{-2}}$ in 1-250 keV, which is far below the sensitivity limits of the X-ray telescopes currently in orbit (or in the foreseeable future). This may explain the non-detection of the X-ray counterpart of any cosmological FRB so far. Nevertheless, our identification of FRB 200428 with a magnetar means at least some of FRBs are produced by magnetars, thus FRBs can be used as an effective tool to study the extra-galactic magnetars, which are otherwise undetectable. On the other hand, giant flares from magnetars can have peak luminosity of $10^{44-47}\ \mathrm{erg\ s^{-1}}$, about 4–7 orders of magnitude more luminous than this non-thermal X-ray burst, and thus might be detectable with the current X-ray telescopes in orbit or the future X-ray missions, such as eXTP[30] which has a much larger effective area in the X-ray band than those X-ray telescopes in orbit. A giant flare of a magnetar might not be associated with an FRB by temporal coincidence, however, the peak of a magnetar giant flare as a short X-ray transient event may be detected from the same direction of an FRB (previously detected or to be discovered in the future) and thus identified as the counterpart of the FRB.

1. Lorimer, D. R., Bailes, M., McLaughlin, M. A., Narkevic, D. J. & Crawford, F. A Bright Millisecond Radio Burst of Extragalactic Origin. Science **318**, 777 (2007).

2. Spitler, L. G. et al. A repeating fast radio burst. Nature **531**, 202–205 (2016).

3. Petroff, E., Hessels, J. W. T. & Lorimer, D. R. Fast radio bursts. Astronomy and Astrophysics Reviews **27**, 4 (2019).

4. Kouveliotou, C. et al. An X-ray pulsar with a superstrong magnetic field in the soft γ-ray repeater SGR1806 - 20. Nature **393**, 235–237 (1998).

5. Turolla, R., Zane, S. & Watts, A. L. Magnetars: the physics behind observations. A review. Reports on Progress in Physics **78**, 116901 (2015).

6. Camilo, F. et al. Transient pulsed radio emission from a magnetar. Nature **442**, 892–895 (2006).

7. Tendulkar, S. P., Kaspi, V. M. & Patel, C. Radio Nondetection of the SGR 1806-20 Giant Flare and Implications for Fast Radio Bursts. Astrophys. J. **827**, 59 (2016).

8. The CHIME/FRB Collaboration et al. A bright millisecond-duration radio burst from a Galactic magnetar. arXiv e-prints arXiv:2005.10324 (2020).

9. Bochenek, C. D. et al. A fast radio burst associated with a Galactic magnetar. arXiv e-prints arXiv:2005.10828 (2020).

10. Zhang, S.-N. et al. Overview to the Hard X-ray Modulation Telescope (Insight-HXMT) Satellite. Science China Physics, Mechanics, and Astronomy **63**, 249502 (2020).

11. Israel, G. L. et al. The discovery, monitoring and environment of SGR J1935+2154. Mon. Not. R. Astron. Soc. **457**, 3448–3456 (2016).

12. Younes, G. et al. X-Ray and Radio Observations of the Magnetar SGR J1935+2154 during Its 2014, 2015, and 2016 Outbursts. Astrophys. J. **847**, 85 (2017).

13. Lin, L. et al. Burst Properties of the Most Recurring Transient Magnetar SGR J1935+2154. Astrophys. J. **893**, 156 (2020).

14. Kozlova, A. V. et al. The first observation of an intermediate flare from SGR 1935+2154. Mon. Not. R. Astron. Soc. **460**, 2008–2014 (2016).

15. Palmer, D. M. & BAT Team. A Forest of Bursts from SGR 1935+2154. GRB Coordinates Network **27665**, 1 (2020).

16. Younes, G. et al. Burst forest from SGR 1935+2154 as detected with NICER. The Astronomer's Telegram **13678**, 1 (2020).

17. Mereghetti, S. et al. SGR 1935+2154: INTEGRAL hard X-ray counterpart of radio burst. GRB Coordinates Network **27668**, 1 (2020).

18. Ridnaia, A. et al. Konus-Wind observation of hard X-ray counterpart of the radio burst from SGR 1935+2154. GRB Coordinates Network **27669**, 1 (2020).

19. Kothes, R., Sun, X., Gaensler, B. & Reich, W. A Radio Continuum and Polarization Study of SNR G57.2+0.8 Associated with Magnetar SGR 1935+2154. Astrophys. J. **852**, 54 (2018).

20. Katz, J. I. Coherent emission in fast radio bursts. Phys. Rev. D. **89**, 103009 (2014).

21. Kumar, P., Lu, W. & Bhattacharya, M. Fast radio burst source properties and curvature radiation model. Mon. Not. R. Astron. Soc. **468**, 2726–2739 (2017).

22. Yang, Y.-P. & Zhang, B. Bunching Coherent Curvature Radiation in Three-dimensional Magnetic Field Geometry: Application to Pulsars and Fast Radio Bursts. Astrophys. J. **868**, 31 (2018).

23. Lyubarsky, Y. A model for fast extragalactic radio bursts. Mon. Not. R. Astron. Soc. **442**, L9–L13 (2014).

24. Plotnikov, I. & Sironi, L. The synchrotron maser emission from relativistic shocks in Fast Radio Bursts: 1D PIC simulations of cold pair plasmas. Mon. Not. R. Astron. Soc. **485**, 3816–3833 (2019).

25. Thompson, C. & Duncan, R. C. The soft gamma repeaters as very strongly magnetized neutron stars - I. Radiative mechanism for outbursts. Mon. Not. R. Astron. Soc. **275**, 255–300 (1995).

26. Israel, G. L. et al. A Swift Gaze into the 2006 March 29 Burst Forest of SGR 1900+14. Astrophys. J. **685**, 1114–1128 (2008).

27. Lin, L. et al. Broadband Spectral Investigations of SGR J1550-5418 Bursts. Astrophys. J. **756**, 54 (2012).

28. Guidorzi, C. et al. A search for prompt γ-ray counterparts to fast radio bursts in the Insight-HXMT data. Astron. Astrophys. **637**, A69 (2020).

29. Marcote, B. et al. A repeating fast radio burst source localized to a nearby spiral galaxy. Nature **577**, 190–194 (2020).

30. Zhang, S. et al. The enhanced X-ray Timing and Polarimetry mission—eXTP. Science China Physics, Mechanics, and Astronomy **62**, 29502 (2019).

Acknowledgements This work made use of the data from the *Insight*-HXMT mission, a project funded by China National Space Administration (CNSA) and the Chinese Academy of Sciences (CAS). The *Insight*-HXMT team gratefully acknowledges the support from the National Program on Key Research and Development Project (Grant No. 2016YFA0400800) from the Minister of Science and Technology of China (MOST) and the Strategic Priority Research Program of the Chinese Academy of Sciences (Grant No. XDB23040400). The authors thank supports from the National Natural Science Foundation of China under Grants U1838105, U1838111, U1838113, U1838202, 11473027, 11733009, U1838201, 1173309, U1838115, U1938109, Y829113, 11673023, U1838104, 11703002

Competing Interests The authors declare that they have no competing financial interests.

Author Contributions CKL, LL and SLX are co-first authors and listed in alphabetical order. TPL, FJL and SNZ are co-corresponding authors and listed in alphabetical order. TPL was the initial proposer and PI of *Insight*-HXMT. SNZ is the current PI of *Insight*-HXMT, organized the observations, data analysis and presentation of the results, writing and editing of the paper. LL proposed the ToO observation, is a main writer of the paper and participated in discussions. SLX participated in organizing the observations, data analysis, discussion and paper writing. FJL is a leader in building *Insight*-HXMT and participated in organizing the data analysis, discussions and paper writing. CKL is the main contributor to the data analysis and participated in paper writing. BZ is responsible for theoretical interpretation, and participated in organizing the observations, discussions, and paper writing. MYG, YLT, XBL, YN, SX, YC, LMS, YT, XFZ, CZL, SMJ, JYL and BL participated in the data analysis and discussion. All other authors contributed to developing, building and operating the *Insight*-HXMT payloads and science data center.

Correspondence Correspondence and requests for materials should be addressed to (T.P.L., F.J.L. and S.N.Z., email: litp@ihep.ac.cn, lufj@ihep.ac.cn, zhangsn@ihep.ac.cn).

Methods

***Insight*-HXMT observations and burst search** The *Insight*-Hard X-ray Modulation Telescope (*Insight*-HXMT) is China's first X-ray astronomy satellite[10,31,32] which was launched on June 15th, 2017. It has an altitude of 550 km and an inclination of 43 degrees. As a broadband X-ray (1–250 keV) observatory, *Insight*-HXMT consists of three telescopes, i.e., the High Energy X-ray telescope (HE) using 18 NaI(Tl)/CsI(Na) phoswich scintillation detectors for 20–250 keV[33], the Medium Energy X-ray telescope (ME) using 1728 Si-PIN detectors for 5–30 keV[34], and the Low Energy X-ray telescope (LE) using 96 Swept Charge Device (SCD) detectors for 1–15 keV[35]. All three telescopes use slat collimators to confine their Field Of Views (FOVs). In addition to the pointed or scanning observation with the collimators, *Insight*-HXMT can also monitor the all-sky in gamma-ray (0.2–3 MeV) using the CsI scintillation detectors of HE. More details about the *Insight*-HXMT can be found in[10].

A dedicated and long Time of Opportunity (ToO) observation of *Insight*-HXMT was implemented for SGR J1935+2154 from 2020-04-28T07:14:51 to 2020-04-29T00:00:00, and a throughout search for X-ray bursts have been made. The trigger condition for the search is that the count rates of three or more NaI detectors of HE exceeds the background count rate, which is the mean count rate in the previous 10 s, with significance greater than 3σ at five time scales (0.05 s, 0.1 s, 0.2 s, 0.5 s and 1 s). This search results in 11 bursts. The starting time and other properties are listed in Table 1, where the fluence is obtained by fitting their spectra with simple spectral models (i.e. PL or CPL), as the fluence does not varies significantly with which spectral model is used. Saturation and deadtime corrections are made before spectral fitting, according to the procedures described below. More detailed analyses of these bursts will be presented elsewhere.

The rest of this **Methods** part is mainly dedicated to the burst at 2020-04-28T14:34:24.00 (UTC) that is associated with FRB 200428. Because of the extreme brightness, the *Insight*-HXMT data suffers substantial saturation and deadtime effects, which require dedicated corrections as detailed below.

Data analysis The timing and spectral results of the X-ray burst associated with FRB 200428 are obtained by analysing the *Insight*-HXMT 1L data with the *Insight*-HXMT Data Analysis Software package (`HXMTDAS`) version 2.02. Specifically, the steps are: (1) Use the commands `hepical`, `mepical`, `lepical` in `HXMTDAS` to calibrate the photon events from the 1L data according to the Calibration Database (CALDB) of *Insight*-HXMT. As for HE, the short spikes with known characteristics produced in the electronics are removed from the physical events. (2) Select the good time intervals (GTIs) from T_0-0 to T_0+1 s, where T_0 is 2020-04-28 14:34:24 UTC. (3) Extract the good events based on the GTIs using the commands `hescreen`, `mescreen`, and `lescreen`. (4)

Generate the spectrum with the selected events using the commands `hespecgen`, `mespecgen`, and `lespecgen`. (5) Create the background spectrum from the events in the time interval $\mathbf{T}_0 - 51$ to $\mathbf{T}_0 - 1\,\mathrm{s}$. (6) Generate the response matrix files required for spectral analysis using the commands `herspgen`, `merspgen`, and `lerspgen`. (7) Produce the raw ME and LE lightcurves using the commands, `melcgen`, and `lelcgen`.

Due to the strong saturation effect in both LE and HE data, the raw data in some time intervals were discarded on-board and their lightcurves need to be corrected as presented below.

Data saturation and deadtime correction Because of the extremely high flux of the burst, the detected events exceeded the storage limits of their on-board data buffer, and so the observed data suffered from saturation. The observational effect of saturation is that in some time intervals the events are lost. Besides the saturation effect, during the procession of an event by the front-end electronics, the detectors sharing the same Physical Data Acquisition Unit (PDAU) can not record any photons, and such an effect is called deadtime. As will be detailed below, both HE and LE suffered strongly from the saturation effects, while the deadtime effects are significant in the HE and ME data. Both the saturation and deadtime need to be corrected when we produce the lightcurves and spectra.

The 18 phoswich X-ray detectors of HE are divided into three groups, each contains six detectors that share one PDAU. Therefore, the three groups of detectors have different event-lost intervals, which are shown in Figures 1, 2 and 3. We correct for the saturation effects in the data of the three groups independently, and then combine them together when we produce the final lightcurve.

The steps of saturation correction for a group of HE detectors are listed as follows: (1) Find the start and stop time of the intervals in which the raw data are not lost. (2) Calculate the deadtime ratio of each detector as a function of time, the details of which can be found in Xiao et al. (2020)[36]. (3) Screen the data in these time intervals to discard the CsI events (anti-coincident events), as well as the events whose energies are out of the selected energy band. Then, the number of NaI events can be obtained for each detector in the group. Using the time intervals selected in the first step and the deadtime ratio calculated in the second step, the true source count rate of each detector in the group can be obtained. (4) Merge the count rate of all detectors in each group and calculate the error of the merged rate. It should be noted that, for the third group (Group ID is 2), as the events of the blinded detector are not used, a factor of 6/5 is used to normalize its count rate, so that the count rates of the three groups can be compared at the same level and combined together to produce the overall HE lightcurve.

ME does not suffer from the saturation effect and the raw data have no time gap. The deadtime of ME can be calculated with HXMTDAS v2.02. The number and ratio of the lost events in $T_0 + 0.37$ and $T_0 + 0.62\,\mathrm{s}$ are also listed in Table 2. The lightcurves before and after deadtime corrections are shown in Figure 4.

LE has three detector boxes and each box contains 32 SCD detectors. The data of each detector box can be processed independently. In the LE data, besides the normal physical events with energies above the on-board threshold, LE also has the forced trigger events, which record the amplitude of the noise or the pedestal offset for each SCD detector in every 32 ms[32]. The count rate of the forced trigger events in each detector box is 1000 counts per second if there is no saturation effect.

The LE lightcurves are then corrected for saturation using the count rate of the recorded forced trigger events. Since the three detector boxes have different saturated time intervals, we reconstructed the LE lightcurve with almost the full time coverage. The lightcurves before and after saturation correction are shown in Figure 5. The deadtime of LE caused by the force trigger events can also be calculated by HXMTDAS, which are listed in Table 2. It is a minor and negligible issue.

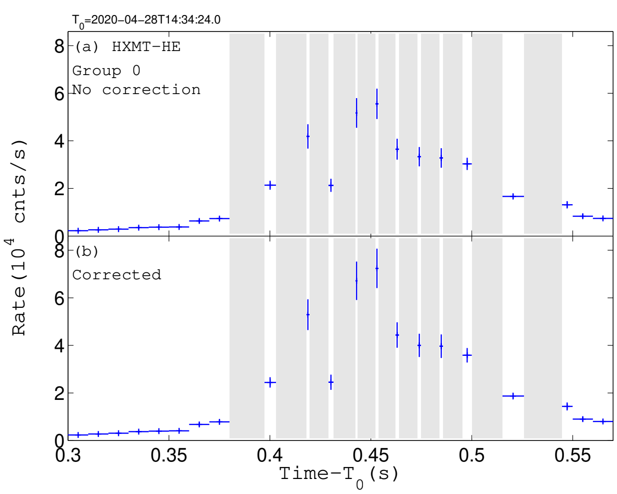

Extended Data Figure 1: The lightcurves of HE group 0. Panel (a): lightcurve before deadtime correction. Panel (b): lightcurve after deadtime correction. The gray belts represent time intervals for the lost events.

Hardness ratio The hardness ratio evolution during the burst is studied by using all the HE, ME and LE data. We derive the 50–250 keV to 27–50 keV hardness ratio with the HE data, and the 10–30 keV to 1–10 keV hardness ratio with the ME and LE data.

To produce the 50–250 keV to 27–50 keV hardness ratio, we first extract photons in 50–

Extended Data Table 1: Bursts detected by *Insight*-HXMT from 2020-04-28T07:14:51 to 2020-04-29T00:00:00. In the table, trigger time is the satellite time, the energy band for fluence calculation is 1–250 keV, duration is that covers 90% of the burst counts, and Δt is the time difference between burst and FRB 200428.

Trigger time (UTC)	Fluence	Duration	Δt
	10^{-8}erg cm^{-2}	s	s
2020-04-28T08:03:34.35	5.65 ± 1.14	0.11	-23458.65
2020-04-28T08:05:50.15	5.04 ± 1.39	0.07	-23322.85
2020-04-28T09:08:44.30	1.37 ± 1.86	0.06	-19548.70
2020-04-28T09:51:04.90	25.58 ± 2.51	0.42	-17008.10
2020-04-28T11:12:58.55	1.30 ± 1.41	0.06	-12094.45
2020-04-28T12:54:02.20	0.87 ± 1.09	0.40	-6030.80
2020-04-28T14:20:52.50	2.93 ± 1.17	0.60	-820.50
2020-04-28T14:20:57.90	2.06 ± 2.45	0.06	-815.10
2020-04-28T14:34:24.00	63.68 ± 6.62	0.53	-9.00
2020-04-28T17:15:26.25	0.25 ± 0.42	0.08	9653.25
2020-04-28T19:01:59.85	3.01 ± 1.22	0.16	16046.85

Extended Data Table 2: Events lost due to saturation and deadtime in $T_0 + 0.37$ and $T_0 + 0.62\,\mathrm{s}$

Telescope	Group ID	N1[a]	LR1[b]	N2[c]	LR2[d]
HE	0	5627	66.0%	981	11.5%
	1	6210	70.8%	1106	12.6%
	2	4793	61.7%	909	11.7%
ME	0	0	0	379	32.8%
	1	0	0	554	47.6%
	2	0	0	688	53.0%
LE	0	276	29.6%	0.26	0.03%
	1	377	35.2%	0.27	0.03%
	2	418	37.6%	0.27	0.03%

[a] N1 is the number of events lost due to saturation.
[b] LR1 is the lost ratio of events due to saturation.
[c] N2 is the number of events lost due to deadtime. For LE, the deadtime is induced by the forced trigger events.
[d] LR2 is the lost ratio of events due to deadtime.

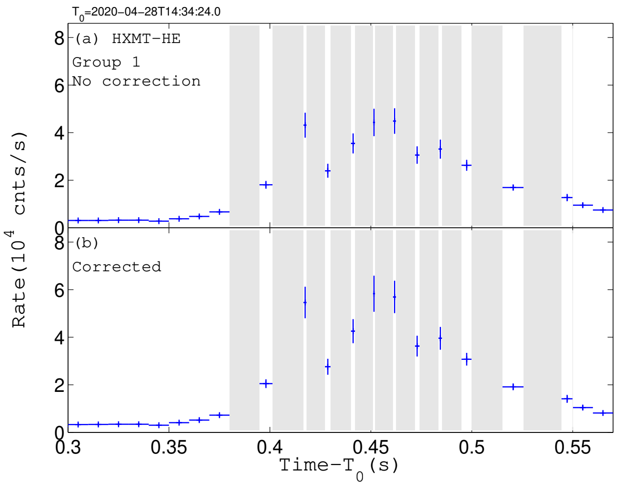

Extended Data Figure 2: The lightcurves of HE group 1. Panel (a): lightcurve before deadtime correction. Penal (b): lightcurve after deadtime correction. The gray belts represent time intervals for the lost events.

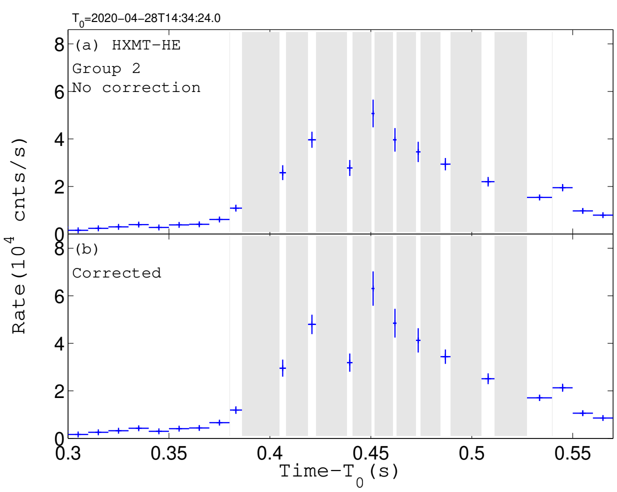

Extended Data Figure 3: The lightcurves of HE group 2. Panel (a): lightcurve before deadtime correction. Panel (b): lightcurve after deadtime correction. The gray belts represent time intervals for the lost events.

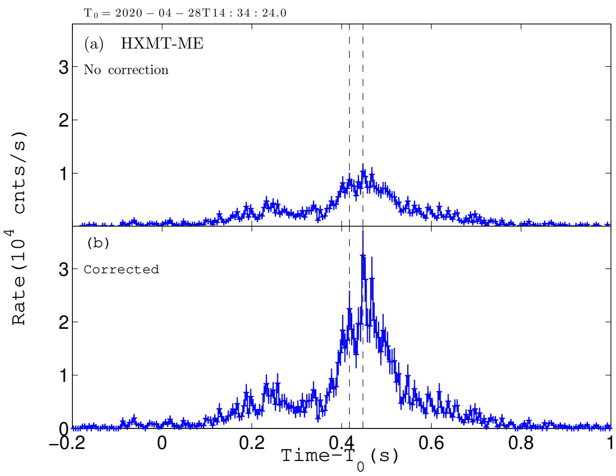

Extended Data Figure 4: The lightcurves of ME. Panel (a): lightcurve without deadtime correction. Panel (b): lightcurve after deadtime correction.

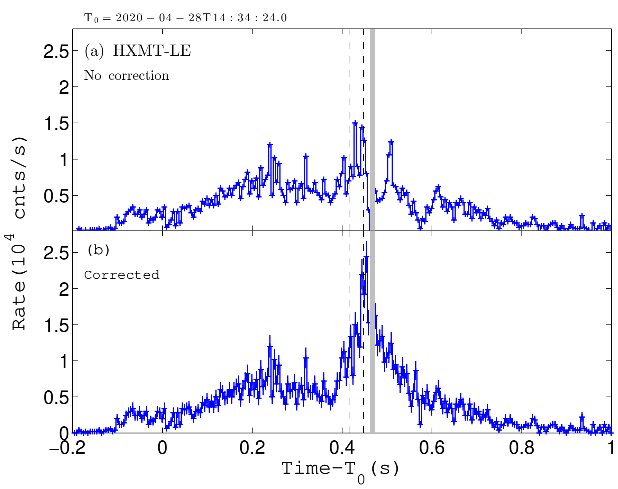

Extended Data Figure 5: The lightcurves of LE. Panel (a): lightcurve before correction of lost events. Panel (b): light curve after lost events correction. The gray belts represent the time interval in which none of the three detector boxes was recording photon events normally.

250 keV and 27–50 keV from the HE data to obtain two lightcurves, in which the bin size before T_0 + 0.38 s and after T_0 + 0.53 s is 60 ms, and the bin size in between is 1 ms. Since the background events contribute to the lightcurves (and so the hardness ratio), especially in the two wings of the burst, we subtract the background of each lightcurve by using the linear interpolation of the count rates in two time intervals before and after the peak, i.e., T_0 - 4 s to T_0 - 2 s and T_0 + 2 s to T_0 + 4 s. The errors of the hardness ratios are calculated with the standard error propagation formula.

The HE data are used in different ways when producing the hardness ratio in different time intervals. Before T_0 + 0.38 s and after T_0 + 0.53 s, the hardness ratio is given by the ratio of the combined lightcurve of the three detector groups, because there is no saturation effect and the count rates can be calculated in the same time bins. However, from T_0 + 0.38 s to T_0 + 0.53 s, the three detector groups have different data gaps caused by the saturation effect, and so the hardness ratio data points are calculated for each of the three group, respectively.

The hardness ratio between ME and LE is calculated by the ratio of the counts rate in 10–30 keV and 1–10 keV. The time bin width for the hardness ratio calculation in this energy band is 10 ms. A possible background contribution to the hardness ratio is also subtracted.

The two narrow peaks As shown in Figure 2, the lightcurve in each energy band roughly consists of two bumps located at around T_0+0.2 and T_0+0.45 s, and the HE and ME lightcurves show two narrow peaks on the second main bump. In order to estimate the significance and to get the exact time of each peak, the HE and ME lightcurves are fitted by five Gaussian functions, in which two of them are used to describe the two narrow peaks,

$$R = N_{\rm p1}G(t, t_{\rm p1}, \sigma_{\rm p1}) + N_{\rm p2}G(t, t_{\rm p2}, \sigma_{\rm p2}) + R_3, \tag{1}$$

where $G(t, t_{\rm p}, \sigma_{\rm p}) = \frac{1}{\sqrt{2\pi}\sigma_{\rm p}} \exp(-\frac{(t-t_{\rm p})^2}{2\sigma_{\rm p}^2})$, $N_{\rm p1}$ and $N_{\rm p2}$ are the normalization, $t_{\rm p1}$ and $t_{\rm p2}$ are the arrival times of the two narrow peaks, $\sigma_{\rm p1}$ and $\sigma_{\rm p2}$ are the Gaussian widths of the two narrow peaks. $R_3 = \sum_{i=3}^{5} G(t, t_{\rm pi}, \sigma_{\rm pi}) + l$ describes the three Gaussian functions for the broad components of the lightcurve, where l is the background level of the lightcurve. From the fitting results, the separation τ of the two narrow peaks is calculated from $t_{\rm p2} - t_{\rm p1}$.

As shown in Figure 6 (a) and (b), the lightcurves of HE and ME could be well fitted by equation 1. If the normalization of the two narrow components is set to 0, the reduced-χ^2 is 4.1 (d.o.f.=30) for the fitting to the data points in T_0+0.35 to T_0+0.43 s that contains the first narrow peak. Similarly, the reduced-χ^2 is 3.0 (d.o.f.=29) for duration T_0+0.43 to T_0+0.50 s that contains the second narrow peak. These large reduced-χ^2 values verify the high detection significance of the two narrow peaks.

As shown in Figure 6 (c), the lightcurve of LE can be well fitted by $R = N_{\rm p2}G(t, t_{\rm p2}, \sigma_{\rm p2}) +$

R_3. A narrow peak corresponding to the second narrow peak in HE and ME lightcurves is also visible, though not as significant as in HE and ME lightcurves.

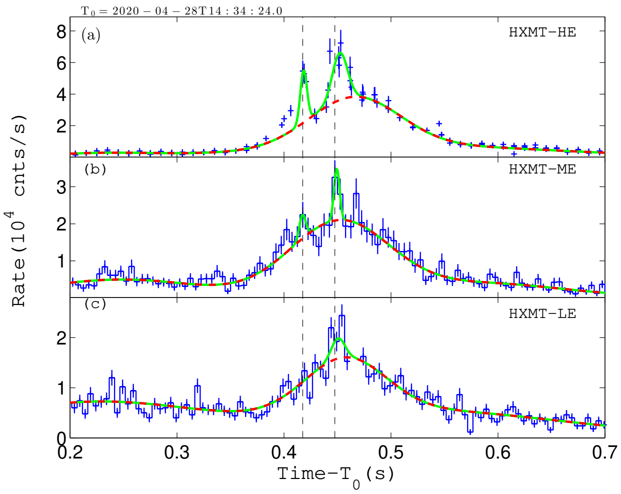

Extended Data Figure 6: Fitting to the lightcurves. The blue points are lightcurves obtained from *Insight*-HXMT HE/ME/LE. The vertical dashed lines are the arrival times of the narrow peaks. The red lines represent the sum of the three broad Gaussian functions. In panels (a) and (b), the green lines represent the fitted curves with the sums of the five Gaussian functions for ME and HE, in which two are for the two narrow peaks. In panel (c), the green line represents the fitted curve to the LE lightcurve with four Gaussian functions, in which one is for the narrow peak in coincidence to the second peak in HE and ME lightcurves.

Spectral analyses and model comparison We extract the spectrum using data in a duration of 1.2 s, from T_0 - 0.2 s to T_0 + 1 s. Deadtime correction is a built-in function of the `HXMTDAS` and has been considered in spectral analysis. However, the saturation correction is not implemented in spectrum generation but will be dealt with in spectral fitting process.

We use XSPEC version 12.10.0c to analyze the spectra. Four different models are used to fit the spectra, which are (1) single power-law (PL), (2) cutoff power-law (CPL) , (3) two blackbody (BB+BB) and (4) blackbody plus power-law (BB+PL). In addition, we use a constant ($const$) to represent the saturation effect in LE and HE and the $wabs$ model to account for the absorption of the interstellar medium. Eventually, the four models are: $wabs * cutoffpl * const$, $wabs * pow * const$, $wabs*(bb+bb)*const$ and $wabs*(bb+pow)*const$. The best-fit parameters and their uncertainties are listed in Table 4. The distribution of the fitted residuals is displayed in Figure 2 of the main article.

From Table 4 and Figure 2 of the main article we can easily reject the single power-law model and the two temperature blackbody model, but the cutoff power-law (CPL) and the blackbody plus power-law model (BB+PL) fit the burst spectra well, though the latter has relatively higher χ^2 values and slightly structured residual above 80 keV. Discussions about these models can be found in the main article.

Localization Although the three telescopes of *Insight*-HXMT point to the same nominal directions, the long axis directions of their Field Of Views (FOVs) are different, which could be used to locate the burst. Figure 7 shows the FOVs of the three telescopes of *Insight*-HXMT. Every telescope has three groups of FOVs whose long axis directions are 60 degree different from the neighbouring ones. When the direction of a source deviates from the center of the FOVs, the count rates on detectors with different FOVs decrease with different slopes, following the shapes of the Point Spread Functions (PSF) [37], which allow us to fit the position of the source using the count rates of the burst on different detectors and their PSFs.

PSFs of all *Insight*-HXMT collimators have been calibrated [37], which are then used to reconstruct the position of the source from the differences of the count rates between different FOVs. This localization method has been extensively tested and verified with *Insight*-HXMT observations [38,39].

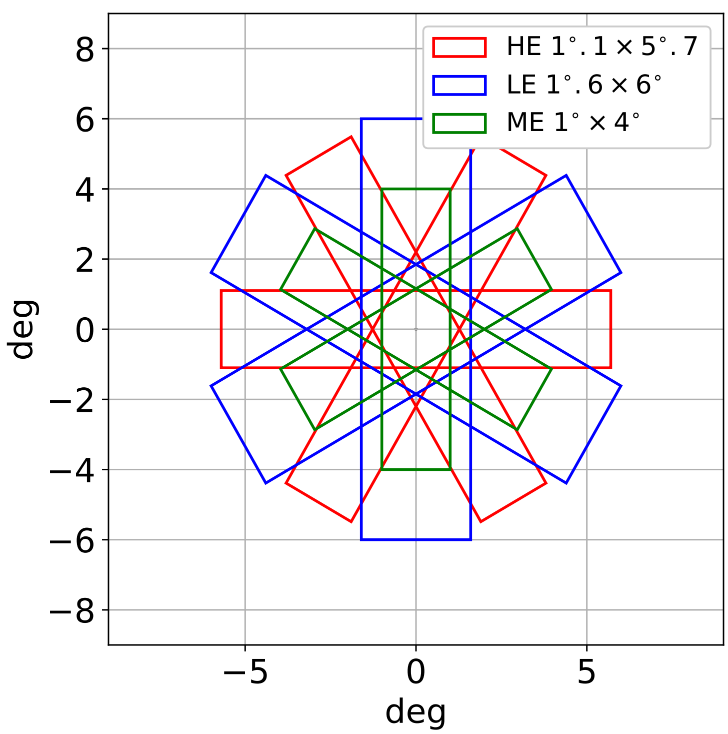

Extended Data Figure 7: The FOVs of LE, ME and HE of *Insight*-HXMT.

For the localization of this burst, count rates of all the three telescopes from UTC 2020-04-28T14:34:24 to UTC 2020-04-28T14:34:25 are used, after saturation and deadtime corrections according to Table 2. In the fitting, for all the the three telescopes the same burst position (RA and Dec) parameters are assumed with three different normalized flux parameters. A Markov Chain Monte Carlo (MCMC) algorithm is utilized in the fitting. The best fitting result gives a reduced χ^2 of 0.845 for 4 degrees of freedom. Figure 1 shows the distributions of position parameters derived from the MCMC approach. The best-fit location of the burst is 3.7 arcmin away from that of SGR J1935+2154 with 1σ uncertainty of 10 arcmin, fully consistent with SGR J1935+2154.

Extended Data Table 3: Fitting parameters of the two narrow peaks for HE and ME, and one narrow (second) peak for LE.

Telescope	t_{p1} (ms)	σ_{p1} (ms)	t_{p2} (ms)	σ_{p2} (ms)	τ (ms)
HE	418 ± 2	3.1 ± 2.7	452 ± 1	7.0 ± 0.8	34 ± 2
ME	417 ± 2	3.0 ± 1.7	449 ± 2	3 ± 3	32 ± 3
LE	–	–	450 ± 2	6 ± 3	–

Extended Data Table 4: Best-fit free parameters of the burst. The integration time for spectrum is from T_0-0.2 s to T_0+1 s. Four models are employed to fit the spectrum observed by *Insight*-HXMT, as cutoff power-law (CPL), power-law (PL), two blackbody (BB+BB), and a model combine blackbody and power-law (BB+PL). $n_{\rm H}$ is the equivalent hydrogen column in the model for interstellar absorption.

Model	$n_{\rm H}$ ($10^{22}{\rm cm}^{-2}$)	kT_1 (keV)	kT_2 (keV)	${\rm Norm}_1$	${\rm Norm}_2$	PhoIndex	$E_{\rm cut}$ (keV)	${\rm factor}_{\rm ME}$	${\rm factor}_{\rm HE}$	$flux_1$ $10^{-7}{\rm erg\ cm}^{-2}{\rm s}^{-1}$	$flux_2$ $10^{-7}{\rm erg\ cm}^{-2}{\rm s}^{-1}$	$\chi^2/d.o.f$
CPL	$2.79^{+0.18}_{-0.17}$	$--$	$--$	$31.48^{+3.50}_{-3.13}$	$--$	$1.56^{+0.06}_{-0.06}$	$83.89^{+9.08}_{-7.55}$	$0.98^{+0.07}_{-0.06}$	$0.68^{+0.07}_{-0.07}$	$5.95^{+0.34}_{-0.32}$	$--$	1.00/242
PL	$4.26^{+0.19}_{-0.18}$	$--$	$--$	$87.26^{+5.17}_{-4.95}$	$--$	$2.21^{+0.03}_{-0.03}$	$--$	$1.68^{+0.08}_{-0.08}$	$1.60^{+0.13}_{-0.13}$	$4.61^{+0.26}_{-0.24}$	$--$	1.48/243
BB+BB	$0.55^{+0.12}_{-0.11}$	$1.63^{+0.04}_{-0.04}$	$14.46^{+0.25}_{-0.24}$	$1.77^{+0.05}_{-0.04}$	$4.37^{+0.46}_{-0.42}$	$--$	$--$	$1.84^{+0.17}_{-0.16}$	$0.45^{+0.05}_{-0.04}$	$1.47^{+0.04}_{-0.04}$	$3.65^{+0.39}_{-0.35}$	2.14/241
BB+PL	$3.50^{+0.17}_{-0.17}$	$11.32^{+0.55}_{-0.56}$	$--$	$1.56^{+0.31}_{-0.27}$	$54.46^{+4.17}_{-3.87}$	$1.93^{+0.04}_{-0.04}$	$--$	$1.05^{+0.08}_{-0.07}$	$0.54^{+0.07}_{-0.06}$	$1.31^{+0.26}_{-0.22}$	$5.80^{+0.32}_{-0.29}$	1.05/241

31. Zhang, S. et al. The insight-HXMT mission and its recent progresses. In Proc. SPIE, vol. 10699 of Society of Photo-Optical Instrumentation Engineers (SPIE) Conference Series, 106991U (2018).

32. Li, X.-B. et al. In-flight calibration of the Insight-Hard X-ray Modulation Telescope. arXiv preprint arXiv:2003.0699 (2020).

33. Liu, CongZhan et al. The High Energy X-ray telescope (HE) onboard the Insight-HXMT astronomy satellite. Science China Physics, Mechanics, and Astronomy **63**, 249503 (2020).

34. Cao, XueLei et al. The Medium Energy X-ray telescope (ME) onboard the Insight-HXMT astronomy satellite. Science China Physics, Mechanics, and Astronomy **63**, 249504 (2020).

35. Chen, Yong et al. The Low Energy X-ray telescope (LE) onboard the Insight-HXMT astronomy satellite. Science China Physics, Mechanics, and Astronomy **63**, 249505 (2020).

36. Xiao, S. et al. Deadtime calculation method of the High Energy X-ray telescope (HE) onboard the Insight-HXMT satellite. Journal of High Energy Astrophysics **26**, 58-64 (2020).

37. Nang, Yi et al. In-orbit calibration to the point-spread function of Insight-HXMT. Journal of High Energy Astrophysics **25**, 39-47 (2020).

38. Sai, Na et al. Methodology and performance of the two-year galactic plane scanning survey of Insight-HXMT. Journal of High Energy Astrophysics **26**, 1-10 (2020).

39. Guan, Ju et al. A modified direct demodulation method applied to Insight-HXMT Galactic plane scanning survey. Journal of High Energy Astrophysics **26**, 11-20 (2020).

Figures

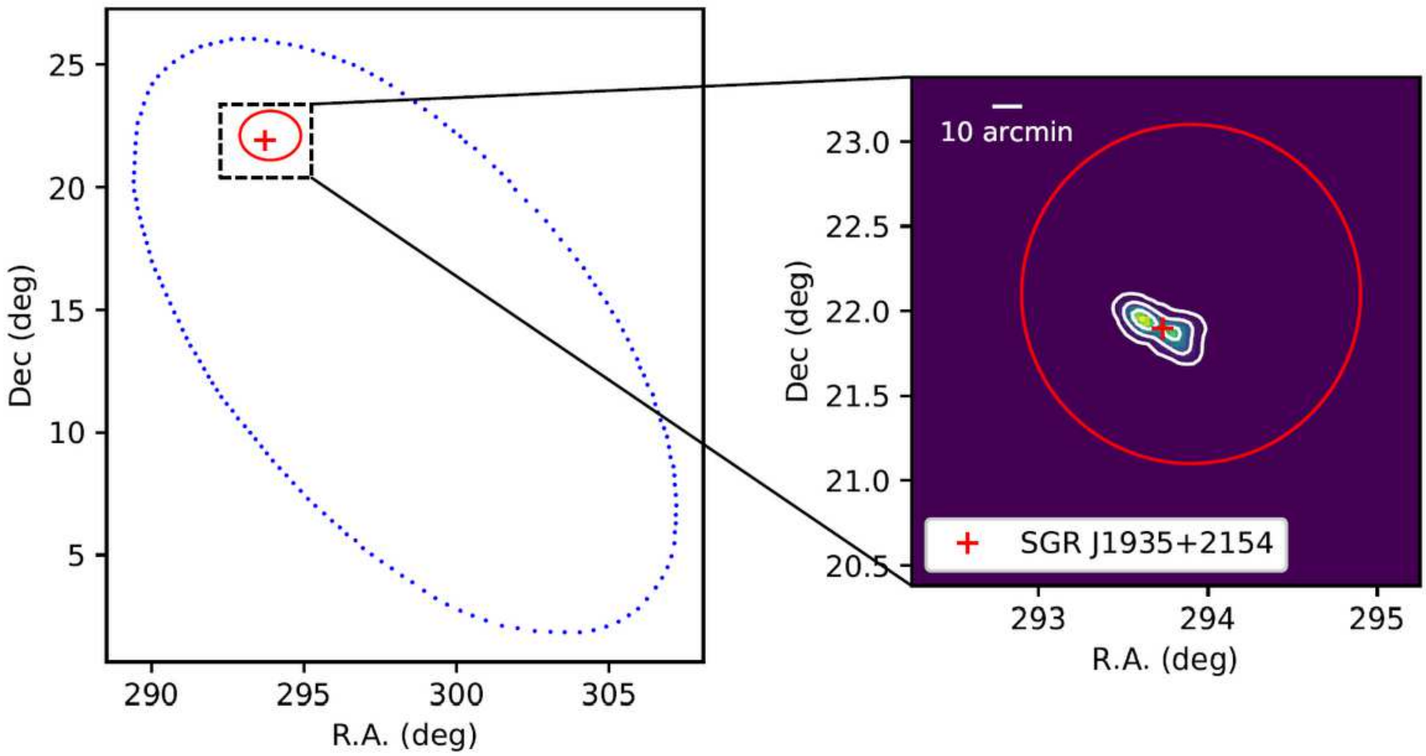

Figure 1

Localization of the burst using Insight-HXMT HE, ME and LE data. The red cross marks the known position of SGR J1935+2154. The white contours in the zoomed in panel are 1, 2 and 3 uncertainty regions in the sky. The best position of this burst is 3.7 arcmin away from SGR J1935+2154 with 1 error of 10 arcmin (see Methods for details about localization). The red circle and blue-dotted ellipse presents the sky region of FRB 200428 determined by CHIME/FRB8 and STARE29, respectively.

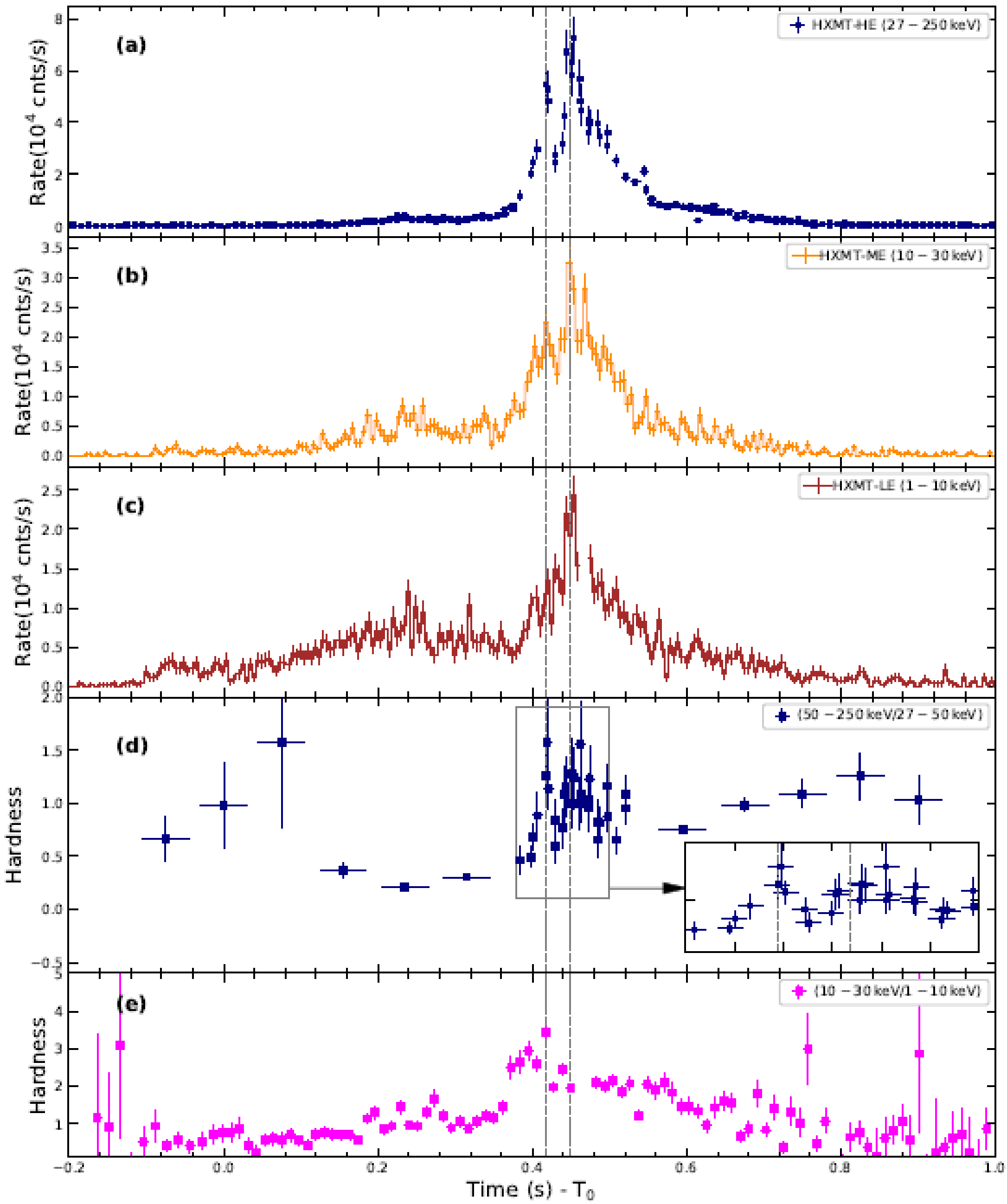

Figure 2

The lightcurve and the hardness evolution during the burst of SGR J1935+2145 observed with Insight-HXMT. The reference time is T0 (2020-04-28 14:34:24 UTC). The vertical dashed lines indicate two peaks in the lightcurves and the hardness evolution. The separation between the two lines are 30 ms. (a): The lightcurve observed with Insight-HXMT/HE with a time resolution of 1 ms near the peak and 10 ms outside the peak. Due to the saturation effect, there are bins near the peak with no photons recorded for both HE and LE. (b) and (c) are the lightcurves observed with ME and LE with a time bin of 5 ms, respectively. (d): The hardness ratio between the counts in 50–250 keV and 27–50 keV. The inset plot in (d) shows the details of the hardness ratio near the peak. (e): The hardness ratio between the counts in 10–30 keV and the 1–10 keV. (see Methods for details of the saturation and the deadtime correction.)

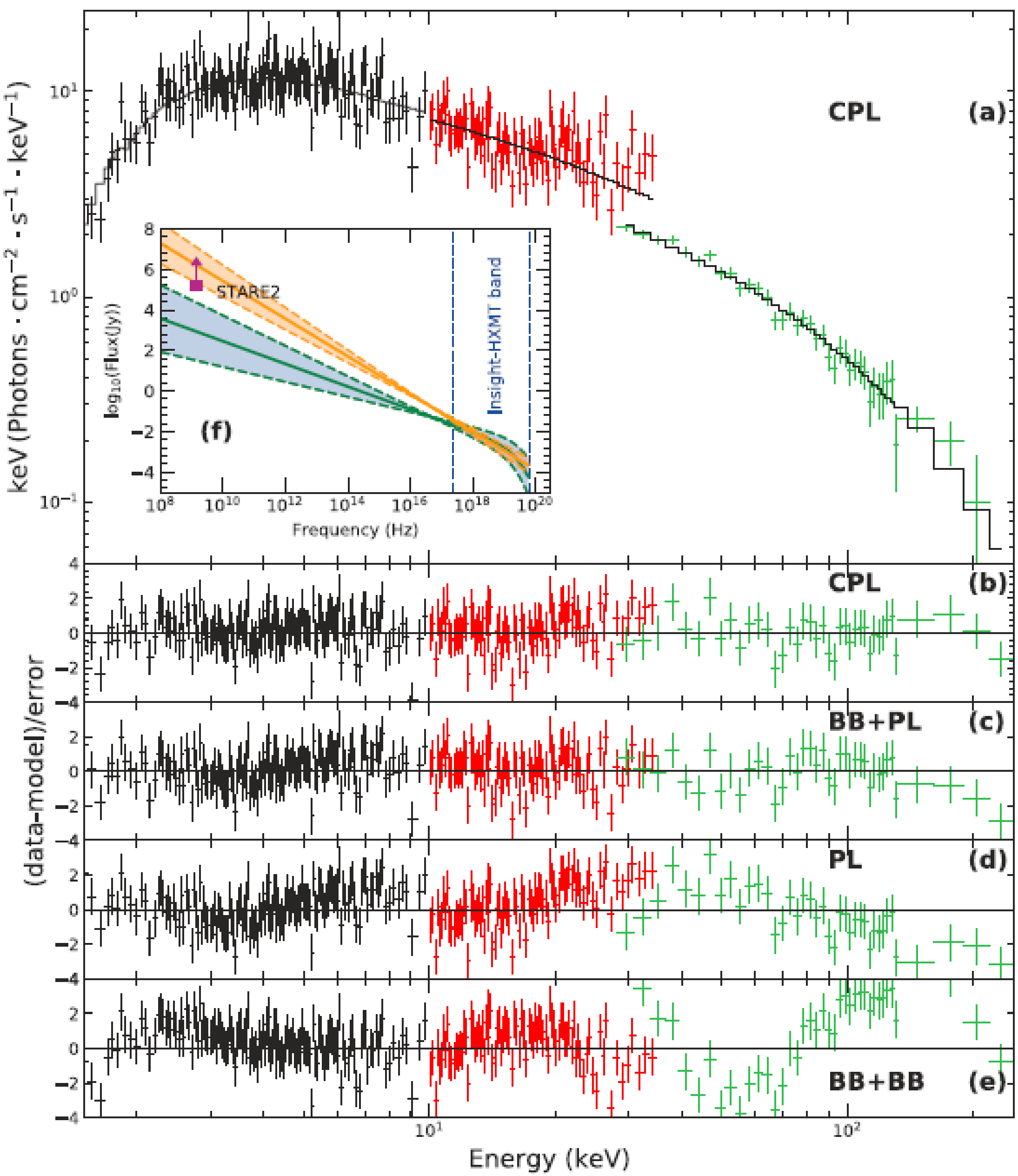

Figure 3

The spectrum observed with Insight-HXMT covers the 1−250 keV energy band. Data from the three telescopes of Insight-HXMT covering different energy bands are represented in different colors (LE: black, ME: red and HE: green). In the fitting process, we introduced a constant factor to offset the different saturation and deadtime effects in different detectors. Four models were considered, cutoff power-law (CPL), blackbody+power-law (BB+PL), power-law (PL), and blackbody+blackbody (BB+BB). The equivalent hydrogen column in the interstellar absorption model was free to fit. (a) The X-ray spectrum of SGR J1935+2154 described by CPL model. The inset (f) shows the comparison between the radio flux lower limit detected with STARE29 and extrapolations from the X-ray spectrum to the radio frequency range, where the green and orange regions are the 3σ error bands with the parameters of the CPL (below

STARE2) and BB+PL (above STARE2) models, respectively. Panels (b)-(e) are the residuals of the data from the individual models, respectively. (see Methods for details of the spectral fitting and parameters derived.)